Engineering Fracture Mechanics 276 (2022) 108940

Contents lists available at ScienceDirect

Engineering Fracture Mechanics

journal homepage: www.elsevier.com/locate/engfracmech

# Effects of specimen geometry and surface defect on high and very high cycle fatigue of TC17 alloy

Han Wu [a,b], Weiqian Chi [c], Wei Xu [d], Wenjing Wang [c], Chengqi Sun [a,b,*]

[a] State Key Laboratory of Nonlinear Mechanics, Institute of Mechanics, Chinese Academy of Sciences, Beijing 100190, China
[b] School of Engineering Science, University of Chinese Academy of Sciences, Beijing 100049, China
[c] Key Laboratory of Vehicle Advanced Manufacturing, Measuring and Control Technology (Beijing Jiaotong University), Ministry of Education, Beijing 100044, China
[d] Beijing Key Laboratory of Aeronautical Materials Testing and Evaluation, Beijing Institute of Aeronautical Materials, Beijing 100095, China

ARTICLE INFO

*Keywords:*
TC17 alloy
Very high cycle fatigue
Surface defect
Specimen geometry
Fatigue strength prediction

ABSTRACT

The column specimen fails from the specimen interior, but the plate specimen fails from the specimen surface for TC17 alloy in very high cycle fatigue. The fatigue strength is lower for plate specimens than that of column specimens for the same surface defect. A model is developed for the fatigue strength $\sigma_{w,\text{column}}$ of the column specimen and the fatigue strength $\sigma_{w,\text{plate}}$ of the plate specimen with approximate plane stress state, i.e., $\sigma_{w,\text{column}} = \sigma_{w,\text{plate}}/(1-\nu^2)$, where $\nu$ is the Poisson ratio. The proposed model for the influence of specimen geometry and surface defect on the fatigue strength accords well with the experimental data.

## 1. Introduction

Very high cycle fatigue (VHCF) has been a hot topic in fatigue research in recent years due to the long-life requirement of many essential parts (e.g., compressor blades of aero-engines). Defects are generally inevitable in the manufacturing process and application of materials and components, which could be incredibly harmful to the fatigue resistance of materials [1–5]. Many results have shown that the fatigue fracture surface of VHCF cracking from internal defects usually presents a fine granular area (FGA) or rough area (i.e., the crack surface is relatively rough from the SEM image compared with its surrounding regions) feature around the defect. And nanograins are often observed for the microstructure in the FGA or rough area [6–10]. However, for VHCF failure due to artificial surface defects, the nanograins were not observed for the structural steel [11] and the TC17 alloy [4] in the VHCF regime. Some models have also been developed for the influence of defects on fatigue performance [2,5,12–14]. For example, Murakami [1] proposed the $\sqrt{area}$ parameter to correlate the result of the small defect on fatigue strength. Chi et al. [15] incorporated the influence of defects in the S-N curve with a bilinear relation. They proposed a model for the influence of artificial surface defects on the fatigue strength in high cycle fatigue (HCF) and VHCF regimes.

As is well known, there are many factors influencing fatigue behavior. For example, the fatigue performance of large-scale specimens (i.e., specimens with the larger high-stress region) is generally poorer than that of small-scale ones [16–20]. Due to stress gradient, the fatigue property in materials under rotating bending loading is higher than that under axial loading for the same local maximum stress [21–23]. The specimen geometry also has an essential effect on fatigue performance [24]. For the same length and size

* Corresponding author at: State Key Laboratory of Nonlinear Mechanics, Institute of Mechanics, Chinese Academy of Sciences, Beijing 100190, China.
*E-mail address:* scq@lnm.imech.ac.cn (C. Sun).

https://doi.org/10.1016/j.engfracmech.2022.108940
Received 21 September 2022; Received in revised form 10 November 2022; Accepted 12 November 2022
Available online 17 November 2022

of the cross-section area in the gauge section, specimens with square cross section present shorter dwell fatigue life than those with circular cross-section [25]. Therefore, it is essential to reveal the influence of both the specimen geometry and defect on VHCF behavior, which will be of great help for fatigue performance evaluation of engineering materials and structures.

This paper focuses on the influence of specimen geometry and artificial surface defect on the HCF and VHCF behavior of TC17 alloy. At first, both column specimens and plate specimens with and without surface defects are tested by an ultrasonic frequency fatigue machine. Then, the fracture surface morphologies are compared for smooth specimens and specimens with surface defects using a scanning electron microscope (SEM). The fracture surface morphologies are also compared for the column specimen and the plate specimen with surface defects by white light interferometry (WLI). Further, several micro samples are extracted in crack initiation and early growth region to reveal the microstructure characteristic by transmission electron microscope (TEM) and transmission Kikuchi diffraction (TKD), and the influence of defects on the crack initiation mechanism of specimens with different geometries is discussed. Finally, the effects of both specimen geometry and defect on the fatigue strength are modeled, and a simple formula is proposed for the difference between column specimens and plate specimens with an approximate plane stress state.

## 2. Testing materials and methods

### 2.1. Materials

The tested material is a TC17 titanium alloy with basketweave microstructure in this paper [4,26,27]. Fig. 1 presents its microstructure along the loading direction by electron backscatter diffraction (EBSD) observation.

### 2.2. Testing methods and microstructure characterization

The column specimen and plate specimen are used to study the influence of specimen geometry and defect on HCF and VHCF behavior of the TC17 alloy. For column specimens, three types of samples are used: smooth specimens, specimens with artificial surface defect A, and specimens with artificial surface defect B. For plate specimens, smooth specimens, and specimens with artificial surface defect B are used. Some results for the smooth plate specimen have been shown in Ref. [27], and some results for plate specimens with the artificial surface defect have been shown in Ref. [26]. All defects were fabricated in the smallest cross sections of smooth samples by a drill. The smooth column and plate specimens are illustrated in Fig. 2a and 2b, respectively. The shapes of defect A and defect B are shown in Fig. 2c and 2d, respectively, referring to the fracture surface morphologies of some failed specimens from defects. The defect width $w$, depth $h$, and size $\sqrt{area}$ for the column and plate specimens are shown in Table 1. The average size of the defect is 90 μm for column specimens with defect A, 256 μm for column specimens with defect B, and 209 μm for plate specimens with the defect. The defect size $\sqrt{area}$ is defined as the square root of the defect's projection area on the fatigue fracture surface [1,4], and it is measured for some failed specimens [26].

The fatigue tests were worked out by an ultrasonic frequency fatigue machine [10]. The continuous fatigue loading was conducted, and compressive air was used to cool the specimen during the fatigue test. The frequency is 20,000 Hz, and the stress ratio is –1. The gauge sections were ground and polished for smooth samples before the fatigue test. For specimens with artificial surface defects, the defects were drilled after the gauge sections of samples were polished.

SEM was employed to observe the fatigue fracture surface morphologies, and several micro cross-section samples were extracted in crack initiation and early growth region by focused ion beam technique for both the smooth plate specimen and the column specimen with the artificial surface defect. The extracted samples were then observed by SEM, TKD, and TEM. The WLI was used to measure the fracture surface morphologies by the ZYGO NewView 9000 3D optical surface profiler for a further understanding of the fracture surface characteristic of different shapes of specimens with artificial surface defects.

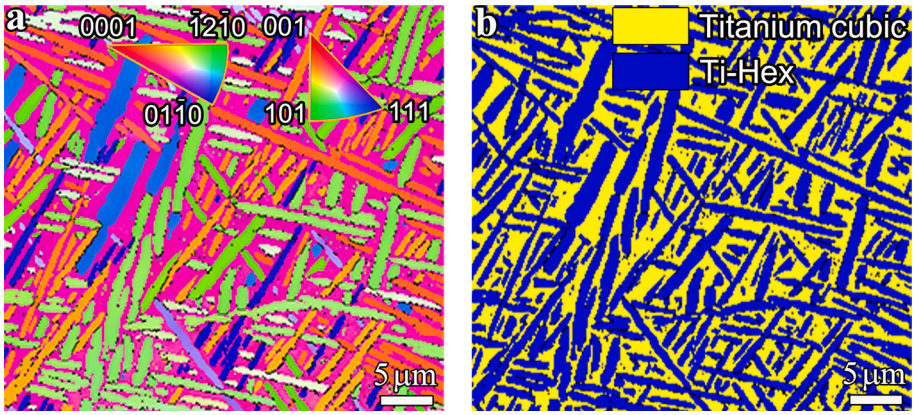


**Fig. 1.** EBSD results of the microstructure. a: Inverse pole figure (IPF); b: Phase map.

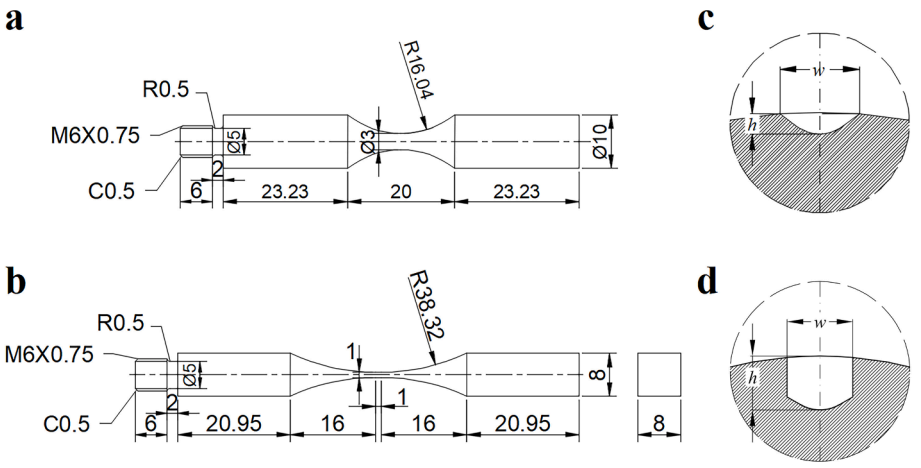


**Fig. 2.** Fatigue specimens. a: Smooth column specimen (mm); b: Smooth plate specimen (mm); c: Sketch map of drilled defect A; d: Sketch map of drilled defect B.

**Table 1**
Defect width $w$, depth $h$, and size $\sqrt{area}$ for the column and plate specimens.

| Specimen type | $w$ (μm) | $h$ (μm) | $\sqrt{area}$ (μm) |
|---|---|---|---|
| Column specimen with defect A | 190 ~ 232 | 50 ~ 56 | 84 ~ 96 |
| Column specimen with defect B | 306 ~ 367 | 201 ~ 254 | 234 ~ 274 |
| Plate specimen with defect | 327 ~ 336 | 141 ~ 171 | 197 ~ 217 |

## 3. Results and analyses

### 3.1. Effects of specimen geometry and defect on fatigue performance

S-N data of column and plate specimens with and without artificial surface defects are presented in Fig. 3. For samples with artificial surface defects, the stress amplitude is taken as that of the corresponding smooth specimen. It is found that the fatigue strength is significantly reduced by the defect for both column and plate specimens. Considering that the defect size (ranging from 234 μm to 274 μm) for column specimens with defect B is larger than that (ranging from 197 μm to 217 μm) for the plate specimen with artificial surface defect and that the larger defect size generally results in the poorer fatigue performance [1,3–5,15], the fatigue performance of column specimens is better than plate specimens for the same artificial surface defect.

The fatigue performance of column specimens with defect B is also compared with that of the column specimens with almost the same drilled defect (the defect size ranges from 233 μm to 287 μm) under the rotating bending fatigue test [4]. The results are

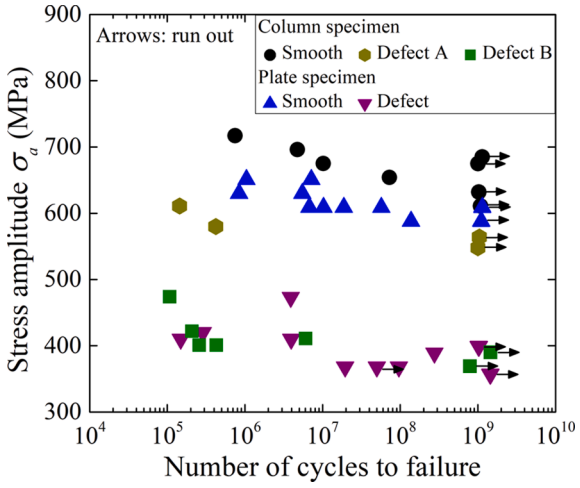


**Fig. 3.** S-N data of smooth specimens and specimens with artificial surface defects.

illustrated in Fig. 4. It is seen that the fatigue performance under the ultrasonic fatigue test is lower than that under the rotating bending fatigue test. For example, the fatigue strength is 395.5 MPa at $10^9$ cycles for column specimens with artificial surface defects under the ultrasonic fatigue test, which is about 13.4 % lower than that (456.5 MPa) of column specimens with artificial surface defects under the rotating bending fatigue test. In Fig. 4, the fatigue strength is taken as the average of the maximum value of specimens that do not fail after $10^9$ cycles and the minimum one of specimens that fail before $10^9$ cycles. For specimens with artificial surface defects under the rotating bending fatigue test, the stress amplitude is the local stress amplitude of the associated smooth specimen. It is thought that one of the main reasons for the difference in the fatigue performance of specimens with artificial surface defects between the rotating bending fatigue test and the ultrasonic fatigue test is attributed to the stress gradient due to the loading method of rotating bending, which results in a lower stress concentration at the defect under rotating bending loading. This result implies that the loading type could have a significant influence on the HCF and VHCF strength of specimens with surface defects.

Here, the surface temperature of the column specimen at the smallest cross section is measured through a thermocouple during the fatigue test [28–30], as illustrated in Fig. 5a. Fig. 5b shows the variation of temperature with the loading cycle. The temperatures stabilize rapidly at all the tested stress amplitudes, and the stable values are close to room temperature. It indicates that, for the present TC17 titanium alloy subjected to ultrasonic fatigue test, the temperature rise of the specimen should have no or negligible effect on the fatigue performance. It is noted that the temperature measurement is stopped when the temperature stabilizes.

### 3.2. *Effects of specimen geometry and defect on fracture surface morphology*

#### 3.2.1. *Column specimen with and without defect*

The cracks of failed smooth column specimens all initiate from the interior of specimens in HCF and VHCF regimes. For Ti alloys, the fracture surface could exhibit a rough area or FGA feature for interior crack-induced fatigue failure [4,5,8]. The rough area characteristic is also found for the present TC17 alloy in HCF and VHCF regimes under the ultrasonic fatigue test, as illustrated in Fig. 6.

For column specimens with artificial surface defects, the cracks of failed samples all originate from the defect. Fig. 7 presents the fracture surface morphologies of two failed samples with the defect. Especially, the rough area characteristic is found in the local region at and near the artificial surface defect for a column specimen with defect A failed at $4.20 \times 10^5$ cycles, as presented in Fig. 7b. This shows that the fatigue fracture surface could also present the rough area feature at the defect for the fatigue failure due to surface defect.

#### 3.2.2. *Plate specimen with and without defect*

Different from smooth column specimens, the failure of smooth plate specimens is due to the surface crack initiation under the ultrasonic fatigue test. All the specimens that failed in the HCF regime have one main crack [27], as illustrated in Fig. 8a-8d. Two samples exhibit “bright area” (i.e., the crack surface is relatively bright but not rough in the SEM image compared with its surrounding regions) features in crack initiation and early growth region (Fig. 8b). While for the failure of specimens in the VHCF regime, one specimen has multiple micro-cracks on the specimen surface (Fig. 8e and 8f). The other specimens have one main crack on the specimen surface, similar to the samples that failed in the HCF regime. The rough area feature is also observed in the crack initiation and early growth region for the specimen that failed in the VHCF regime [27]. This result implies that the specimen geometry has a significant effect on the failure mechanism of the TC17 alloy under the ultrasonic frequency fatigue test. One of the reasons might be attributed to the difference of the stress states between the column specimen and the plate specimen [31–33].

The cracks of failed plate specimens with defects all initiate from the fault. Fig. 9a and 9b presents the fatigue fracture surface

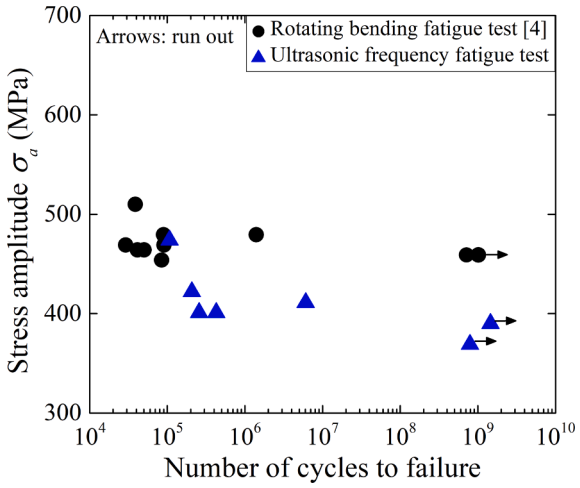


**Fig. 4.** S-N data of present column specimens with defect B by ultrasonic fatigue test and samples with artificial surface defect C by rotating bending fatigue test [4].

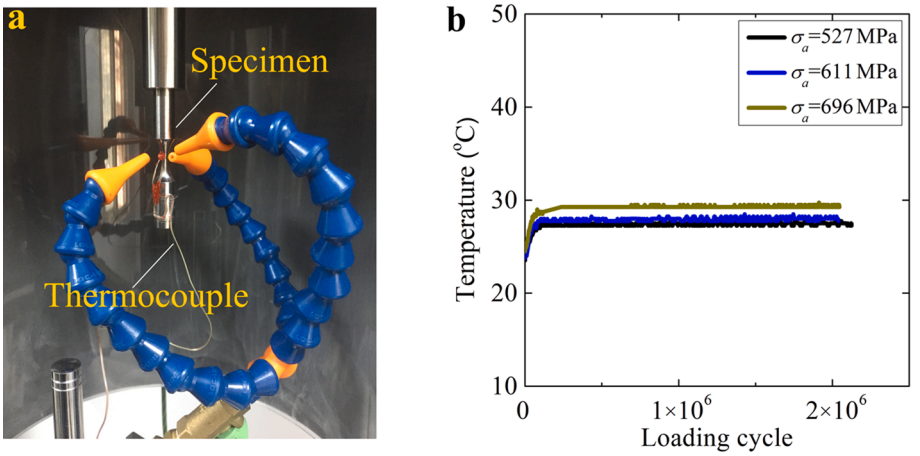


**Fig. 5.** Measurement of temperature during the ultrasonic frequency fatigue test. a: Picture for temperature measurement; b: Variation of temperature versus loading cycle.

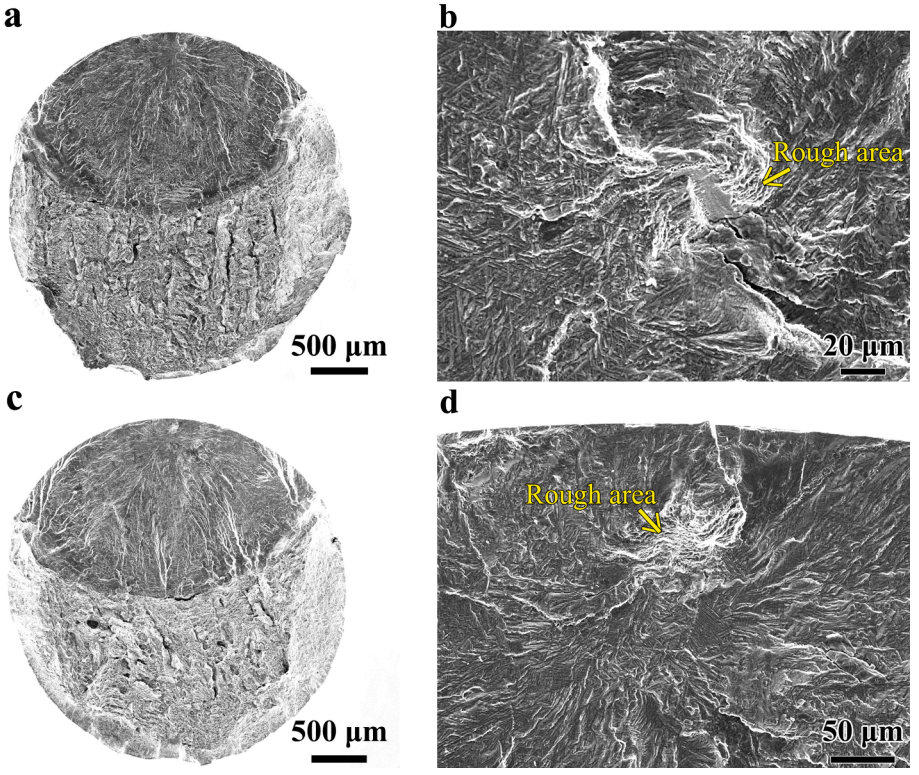


**Fig. 6.** Fracture surface morphologies of smooth column specimens. a and b: $\sigma_a = 696$ MPa and $N_f = 4.72 \times 10^6$ cycles; c and d: $\sigma_a = 675$ MPa and $N_f = 1.02 \times 10^7$ cycles.

morphologies of HCF specimens. Fig. 9c and 9d shows the fracture surface morphologies of VHCF specimens [26]. In comparison with the fracture surface morphologies of column specimens with similar defect (i.e., defect B) in Fig. 7, the fatigue fracture surface near defect is relatively smooth for plate specimens with the surface defect than that for column specimens with surface defects.

### *3.2.3. Fracture surface morphologies by WLI*

The SEM observations in Figs. 7 and 9 indicate that the fracture surface morphologies near the defect have differences for different shapes of specimens with the defect. For further comparison, Fig. 10 shows the fracture surface morphologies for the column specimen with a defect in Fig. 7d and the plate specimen with a defect in Fig. 9b by WLI, respectively. The magnification is ten times. The

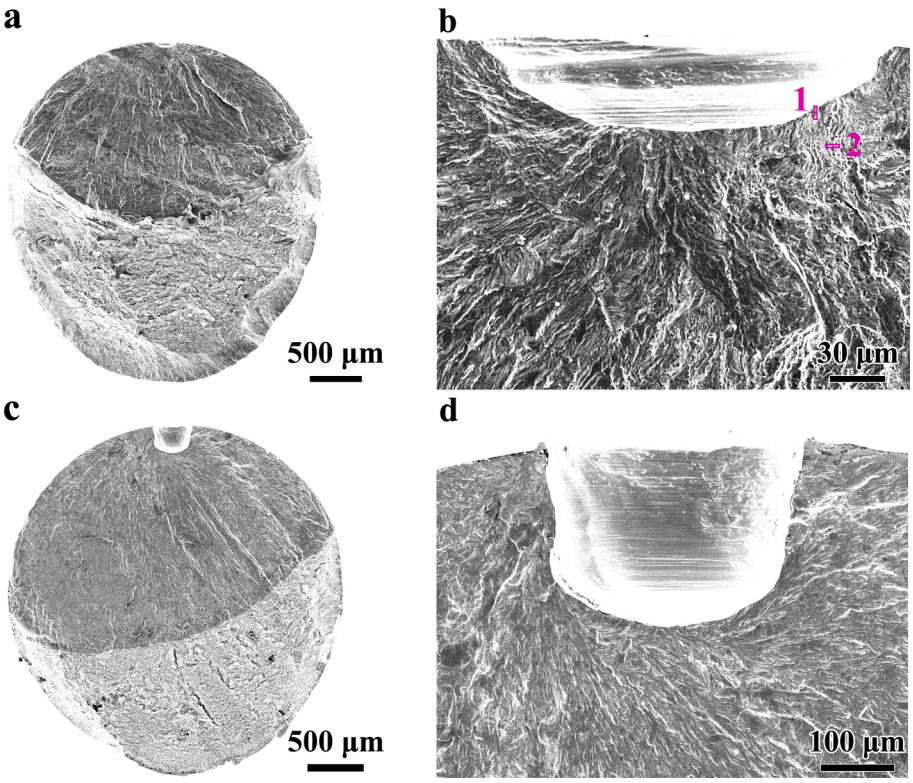


**Fig. 7.** Fracture surface morphologies of column specimens with defects. a and b: Specimen with defect A, $\sigma_a = 580$ MPa and $N_f = 4.20 \times 10^5$ cycles, the rectangles denote the locations where the micro samples 1 and 2 are extracted; c and d: Specimen with defect B, $\sigma_a = 401$ MPa and $N_f = 4.27 \times 10^5$ cycles.

scanning area is 831 μm × 861 μm for the column specimen with defect (Fig. 10a and 10b), and 847 μm × 861 μm for the plate specimen with defect (Fig. 10c and 10d). The reference locations in Fig. 10e and 10f are taken as the positions of C1 and C2, respectively. It is seen from Fig. 10e and 10f that the variation of the height line near the place of C1 is more significant than that of the height line near the place of C2, namely that the fatigue fracture surface near the drilled defect is relatively rougher for the column specimen than that for the plate specimen. This result indicates that the specimen geometry has an important influence on the fracture surface morphology for the TC17 titanium alloy with the artificial surface defect. The difference in fracture surface morphologies should be attributed to the different stress states of the column and plate specimens.

## 4. Discussions

### *4.1. Microstructure characterization in a bright area of the fracture surface*

EBSD results have shown that nanograins formed in α grains in the rough area for HCF and VHCF of the same TC17 alloy [5,27]. Here, the micro-sample is extracted in the bright area along the loading direction. Then, the microstructure is characterized to further understand the formation process of the bright area during fatigue loading. Fig. 8b shows the location of the extracted sample, and Fig. 11a illustrates the SEM observation of the extracted sample. Fig. 11b, Fig. 11c, and Fig. 11d shows the IPF, phase map, and kernel average misorientation (KAM) map of the extracted sample, respectively. The IPF and phase map are not clear for the grains very near the fracture surface, which might be due to the severe plastic deformation or grain refinement of the original grains. Therefore, the TEM observation is further performed, and the selected area diffraction (SAD) patterns are used to characterize the microstructure near the fracture surface. The SAD patterns of diffused rings in Fig. 11e indicate many nano-sized grains with random orientation. Due to that the region for SAD is located in the α phase, there are nano α grains for the microstructure in the bright area in the HCF regime. The results for the same TC17 alloy not experiencing fatigue loading have shown that the nanograins are not found in original α grains [27]. This result indicates that the nano α grains in the bright area are formed due to the cyclic stress, and the nanograin formation could also be crucial for HCF crack initiation and early growth of the present TC17 alloy, similar to that of the VHCF regime [27].

### *4.2. Microstructure characterization in the rough area at defect*

It has been observed that the nanograins appear in some cases for the microstructure in the rough area for the smooth specimens of

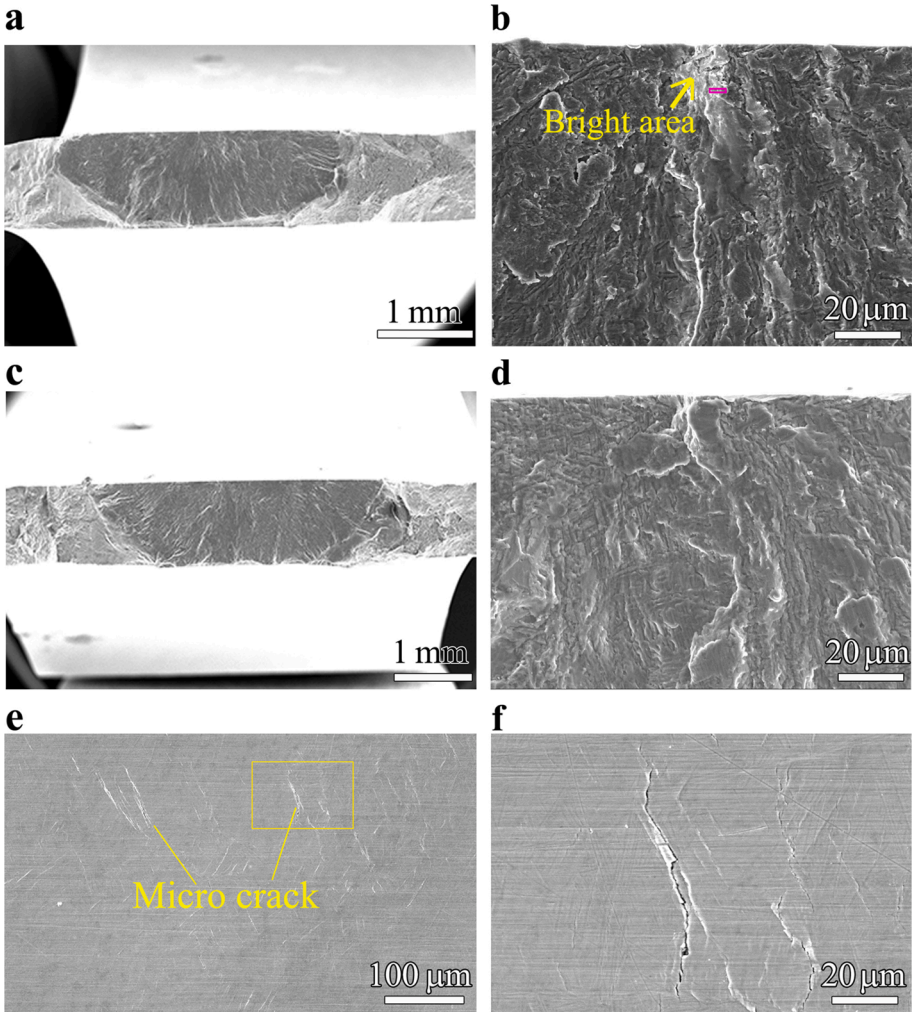


**Fig. 8.** SEM observation of fracture surface and specimen surface with micro-cracks for plate specimens. a and b: Fracture surface, $\sigma_a = 651$ MPa, and $N_f = 7.13 \times 10^6$ cycles, the rectangle denotes the location where the micro sample is extracted; c and d: Fracture surface, $\sigma_a = 630$ MPa, and $N_f = 5.48 \times 10^6$ cycles; e and f: Specimen surface with micro-cracks, $\sigma_a = 588$ MPa and $N_f = 1.37 \times 10^8$ cycles, f is close-up of the rectangular region in e.

Ti alloys failed in HCF and VHCF regimes [4,5,8]. However, the rough area feature has not been reported for the failure of titanium alloys due to surface defects in the HCF or VHCF regime in the literature. Here, two micro samples were extracted in the rough area at and near the defect along the loading direction, and the microstructure was characterized by TKD for the present TC17 alloy. The locations of the extracted samples are illustrated in Fig. 7b, and the observed results are shown in Figs. 12 and 13. It is seen that there are nanograins in grains in the rough area at the artificial surface defect (Figs. 12b and 13b), namely that the nanograin formation could occur for the microstructure in the rough area at the artificial surface defect. The appearance of nanograins was also found in the rough area of smooth samples, which failed from the surface crack initiation for the same TC17 alloy in the VHCF regime [27]. This result implies that the microstructure of the material and the loading condition should be the main factors for the nanograin formation of titanium alloys, and the vacuum environment is not necessary. Furthermore, the KAM map in Figs. 12d and 13d implies that the plastic deformation is severe in α grains where the nanograin forms.

### *4.3. Crack initiation mechanism in the HCF and VHCF regimes*

Persistent slip bands (PSBs) formed during fatigue loads are one of the most essential factors for crack initiation in metals [34,35]. A general belief for the occurrence of this failure mode is that the stress amplitude must exceed the so-called PSB threshold value [36]. However, it has been observed that the cyclic strain localization could develop at a very low-stress amplitude below the PSB threshold value over $10^{10}$ loading cycles [37]. Moreover, the results for Ti alloys and high-strength steels indicate that the nanograin formation due to high local stress is an essential way for VHCF crack initiation [6,9,10,27,38–40]. The grain refinement during the fatigue process increases the local microstructural inhomogeneities. It promotes the fatigue crack initiation (e.g., fatigue crack forms within the

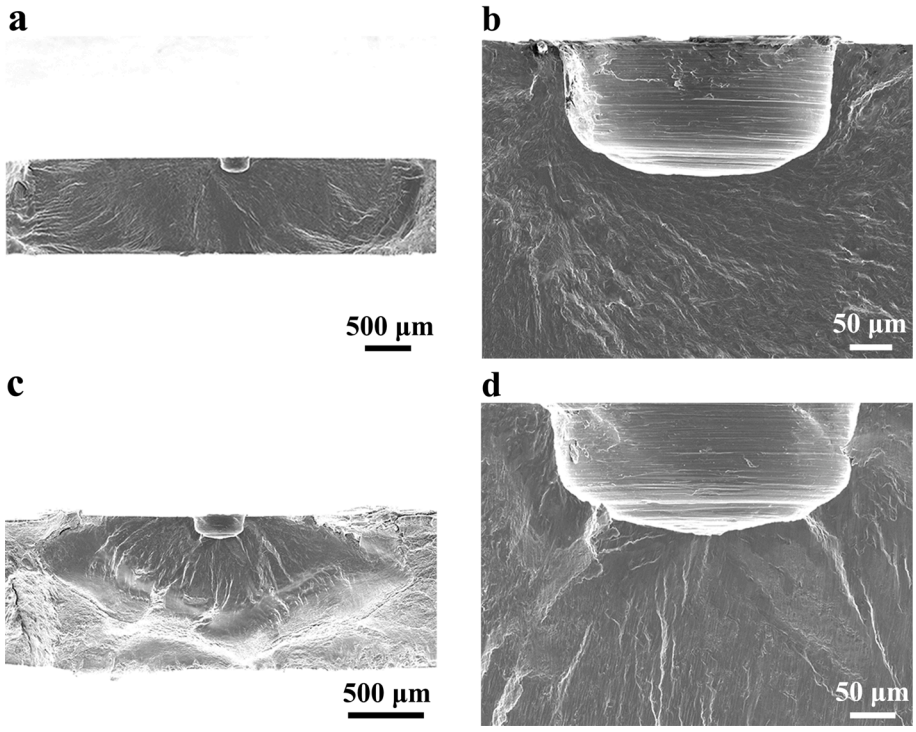


**Fig. 9.** Fracture surface morphologies of plate specimens with defects. a and b: $\sigma_a = 410$ MPa and $N_f = 3.94 \times 10^6$ cycles; c and d: $\sigma_a = 368$ MPa and $N_f = 1.95 \times 10^7$ cycles.

regions of refined grains, at the coarse grain-refined grain boundary) in the VHCF regime [27,41]. This could explain the crack initiation and early growth that accompany the formation of nanograins in VHCF regime [6,9,10,27,38–40]. It is noted that the VHCF crack initiation could also be attributed to the synergistic effect of fatigue stress with time-dependent processes (e.g., the action of hydrogen, the effect of moisture, etc.) during the long time of fatigue loadings [26,42,43]. In this case, the fatigue process is not purely dominated by cyclic stress. The factors (e.g., corrosion, the action of hydrogen, etc.) or the synergistic effect with fatigue loading promotes the crack initiation, and the VHCF fracture surface could not exhibit the slow process of crack initiation and early growth that accompany grain refinement [26].

Regarding the nanograins often present in the crack initiation and early growth region in the VHCF regime, it is thought that the traditional crack initiation, such as that induced by PSB, is usually not satisfied under the low-stress level in the VHCF regime, or a non-propagating micro or small crack is formed during the fatigue loading [26,43]. For this case, the fatigue failure needs some other ways to induce the crack initiation or promote crack growth under the cyclic stress (e.g., the nanograins formed during the cyclic stress reduce the fatigue resistance of materials in local regions in VHCF regime), and it provides a way to promote the fatigue crack initiation and crack growth.

While the stress is relatively higher in the HCF regime, and the fatigue crack tends to nucleate or initiate due to deformation incompatibility and microstructural inhomogeneities (e.g., at defect or inclusion, grain boundaries, etc.). Meanwhile, the grain refinement (e.g., nanograin formation) could occur due to the high local stress during HCF loading. It could also be the prominent contributor to crack nuclei or growth and result in the eventual failure, as indicated in Figs. 11-13. In this case, the failure mechanism is determined by the minimum value of the fatigue life when the grain refinement plays a vital role in the fatigue process (e.g., crack initiation and early growth) and the fatigue life when it is dominated irrespective of grain refinement (e.g., the fatigue failure due to PSB induced crack initiation). If the fatigue life dominated by the grain refinement is shorter than that dominated irrespective of the grain refinement, the microstructure will exhibit (local regions of) refined grain feature in crack initiation and early growth region, as illustrated in Figs. 11-13. Or else, the fatigue failure is dominated irrespective of the grain refinement, and the refined grains are hardly observed at the crack initiation region [11].

According to the results in the literature [41], the titanium with ultrafine grains exhibits superior fatigue performance than that of the titanium with coarse grains in the HCF regime, but their S-N curves merge in the VHCF regime. This result implies that the nanograins tend to restrict HCF crack initiation but promote VHCF crack initiation. It might be the reason why the rough area or FGA often appears in the VHCF crack initiation and early growth region, and the nanograin formation is seldom observed in the crack initiation region for HCF with relatively shorter fatigue life.

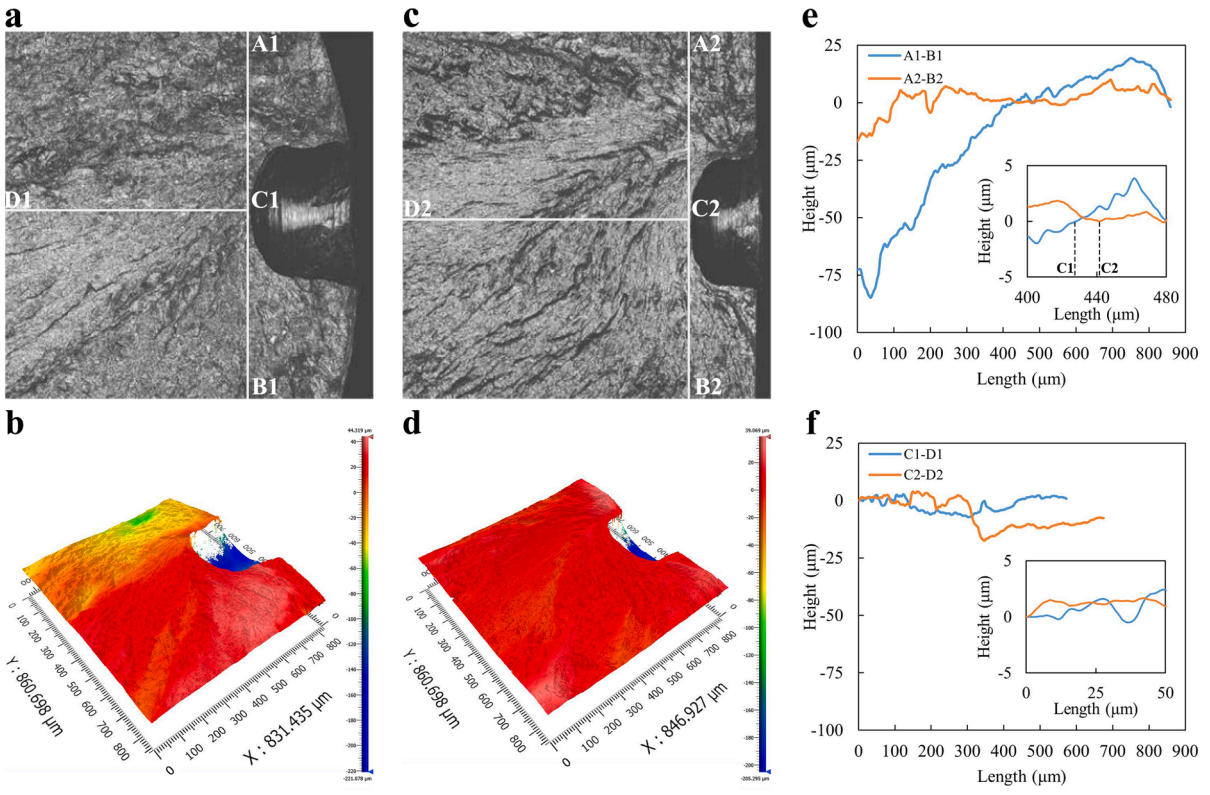


**Fig. 10.** Comparison of fracture surface morphologies by WLI. a and b: SEM and three-dimensional scanning images of the column specimen at $\sigma_a =$ 401 MPa with $N_f = 4.27 \times 10^5$ cycles in Fig. 7d; c and d: SEM and three-dimensional scanning images of the plate specimen at $\sigma_a = 410$ MPa with $N_f = 3.94 \times 10^6$ cycles in Fig. 9b; the lines in a and c denote the locations for the measurement of the height line. e: Height lines along A1-B1 in a and A2-B2 in c, respectively, in which the zero point of the horizontal ordinate corresponds to the positions A1 and A2, respectively. e and f: Height lines along C1-D1 in a and C2-D2 in c, respectively, in which the zero point of the horizontal ordinate corresponds to the positions C1 and C2, respectively. The figures inset in e and f are magnified ones of local regions in e and f, respectively.

### *4.4. Model for effects of specimen geometry and defect on fatigue strength*

The specimen with a larger control surface or control volume (i.e., high-stress region) generally presents poorer fatigue performance compared to the specimen with a smaller one [16–20]. Here, the control surface and control volume are calculated for the smooth column and plate specimens by the theoretical formulas [44], which are taken as the region that is subjected to ≥ 90 % of the maximum principal stress in the smallest cross section of specimens [1,18–20,23]. The control surface and control volume are 33.53 $mm^2$ and 25.63 $mm^3$ for the smooth column specimen, respectively, and 47.14 $mm^2$ and 21.02 $mm^3$ for the plate specimen, respectively. Considering the small difference in the control volume and control surface between the smooth column specimen and smooth plate specimen, the effect of control surface or control volume on the fatigue performance is negligible.

Inspired by the plane stress and plane strain problems, an empirical formula is found for correlating the fatigue strength of the present smooth plate specimen with the approximate plane stress state and that of the smooth column specimen for the same control volume or control surface, i.e.

$$\sigma_{w,\text{column}} = \sigma_{w,\text{plate}}/(1-\nu^2) \tag{1}$$

where $\sigma_{w,\text{column}}$ means the fatigue strength of smooth column specimens, and $\sigma_{w,\text{plate}}$ means the fatigue strength of smooth plate specimens.

Fig. 14 shows the predicted fatigue strengths of smooth column specimens by Eq. (1) with experimental data of smooth plate specimens, in which $\nu$ is taken as 0.334 [45]. The predicted fatigue strengths accord with the experimental ones, which indicates that Eq. (1) is promising for correlating the effect of specimen geometry (column specimen and plate specimen with approximate plane stress state) on HCF and VHCF fatigue strength.

Further, based on the results for the influence of defect on fatigue strength [1,4,5], a model is developed for the effects of specimen geometry and defect, i.e.

$$\alpha\sigma_w = \begin{cases} C\left(\sqrt{area}\right)^n, \sqrt{area} \geq \sqrt{area_0} \\ \alpha\sigma_{w,0}, \sqrt{area} < \sqrt{area_0} \end{cases} \tag{2}$$

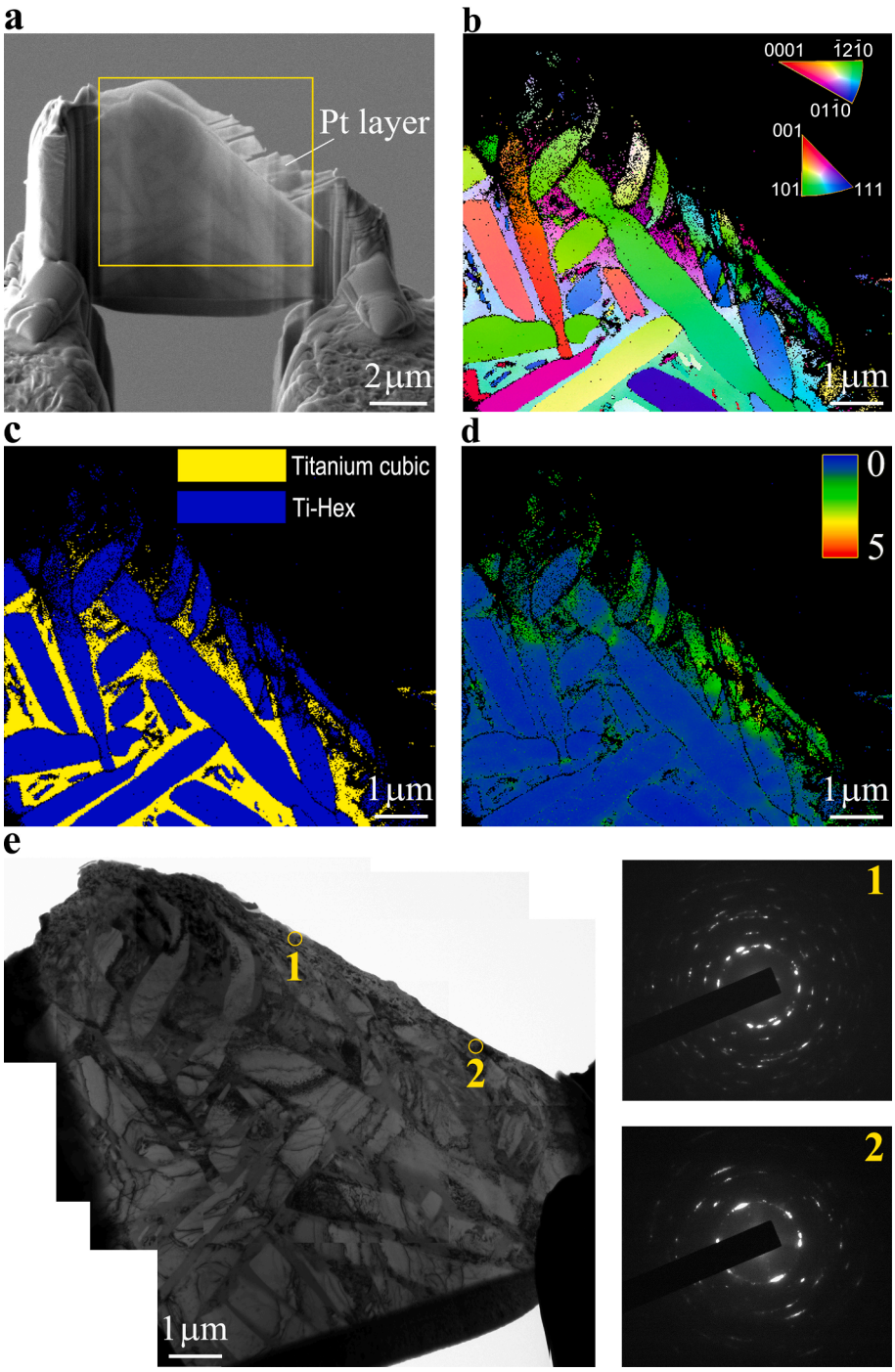


**Fig. 11.** SEM, TKD, and TEM results of the extracted micro-sample in the bright area in Fig. 8b. a: SEM observation of extracted sample; b-d: IPF, phase map, and KAM map of the rectangular region in a, respectively; e: TEM results, the SAD patterns correspond to the circular regions 1 and 2 just beneath the fracture surface, respectively.

where $\sigma_w$ and $\sigma_{w,0}$ denote fatigue strengths of specimens with defect size $\sqrt{area}$ and smooth specimens, respectively, $\sqrt{area_0}$ means the critical defect size smaller than which it has no influence on fatigue strength, $\alpha = 1$ is for column specimen and $\alpha = 1/(1-\nu^2)$ is for plate specimen with approximate plane stress state, $\nu$ is the Poisson ratio, and the parameters $C$ and $n$ could be obtained by using the least square method for $\log_{10}\sigma_w$ smaller than $\log_{10}\sigma_{w,0}$ associated with $\log_{10}\sqrt{area}$.

Fig. 15 compares model results and experimental data for the column and plate specimens with and without artificial surface

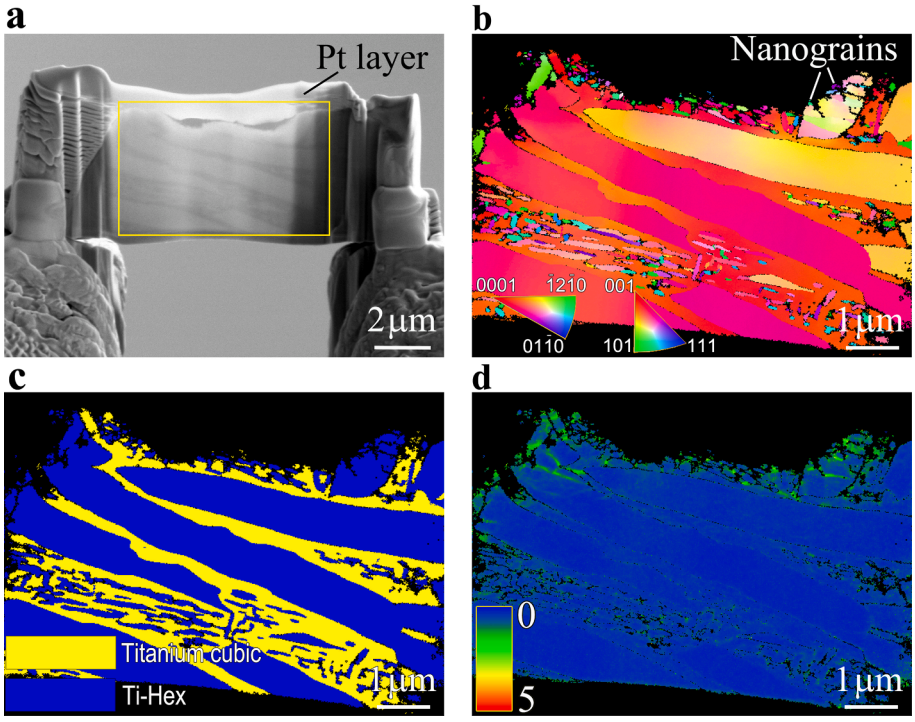


**Fig. 12.** SEM and TKD observation of extracted micro-sample 1 in the rough area in Fig. 7b. a: SEM image of the extracted sample, in which the drilled hole is located on the left of the sample; b-d: IPF, phase map, and KAM map of the rectangular region in a, respectively.

defects on a log–log scale. In Fig. 15, the data for the smooth column and plate specimens are labeled by hollow symbols, and the associated horizontal coordinates are taken as one micron and two microns, respectively. The fatigue strength is obtained in the same way in *Sec*. 3.1. For specimens with defects, the average value of defect sizes is considered. Detailed information on fatigue strength and defect size is shown in Table 2. Here, the experimental data for the column specimen are used to determine the parameters in Eq. (2). The parameters are $n = 0.353$ and $C = 10^{3.4472}$. It is seen that the proposed model by Eq. (2) correlates well with the influence of specimen geometry and defect on the VHCF strength of the TC17 alloy.

It is noted that the residual stress could be introduced in the manufacture of the drilled holes. The residual stress usually has an influence on the fatigue behavior [46]. However, Fig. 15 indicates that the proposed model could reflect the effect of defects on the VHCF strength for the same introduction form of artificial defects. While for the different introduction forms of defects, it should consider the difference of the residual stresses [15,47].

## 5. Conclusions

The influence of specimen geometry and artificial surface defect on HCF and VHCF of TC17 titanium alloy is investigated by ultrasonic frequency fatigue test. The main results are as follows.

(1) The specimen geometry has an essential influence on fatigue performance and crack initiation for HCF and VHCF of TC17 alloy. The column specimen fails from the specimen interior, but the plate specimen fails from the specimen surface. The artificial surface defect significantly reduces the fatigue performance of the TC17 alloy, and the fatigue performance of column specimens is higher than that of plate specimens for the same artificial surface defect.

(2) The rough area feature is found in the local region at defect for a column specimen with the defect that failed in the HCF regime, and nanograins are observed in the rough area. The paper indicates that the nanograin formation in the rough area is independent of specimen geometry, loading type, and crack initiation site.

(3) A model is developed for correlating the effects of specimen geometry and defect on fatigue strength, i.e., $\alpha\sigma_w = \begin{cases} C(\sqrt{area})^n, \sqrt{area} \geq \sqrt{area_0} \\ \alpha\sigma_{w,0}, \sqrt{area} < \sqrt{area_0} \end{cases}$, where $\sigma_w$ and $\sigma_{w,0}$ denote fatigue strengths of specimens with defect size $\sqrt{area}$ and smooth specimens, respectively, $\sqrt{area_0}$ means the critical defect size smaller than which it has no influence on fatigue strength, $\alpha = 1$ is for column specimen and $\alpha = 1/(1-\nu^2)$ is for plate specimen with approximate plane stress state, $\nu$ is the Poisson ratio, and the parameters $C$ and $n$ could be obtained by using the least square method for $\log_{10}\sigma_w$ smaller than $\log_{10}\sigma_{w,0}$ associated with $\log_{10}\sqrt{area}$. The predicted fatigue strengths are in agreement with experimental data.

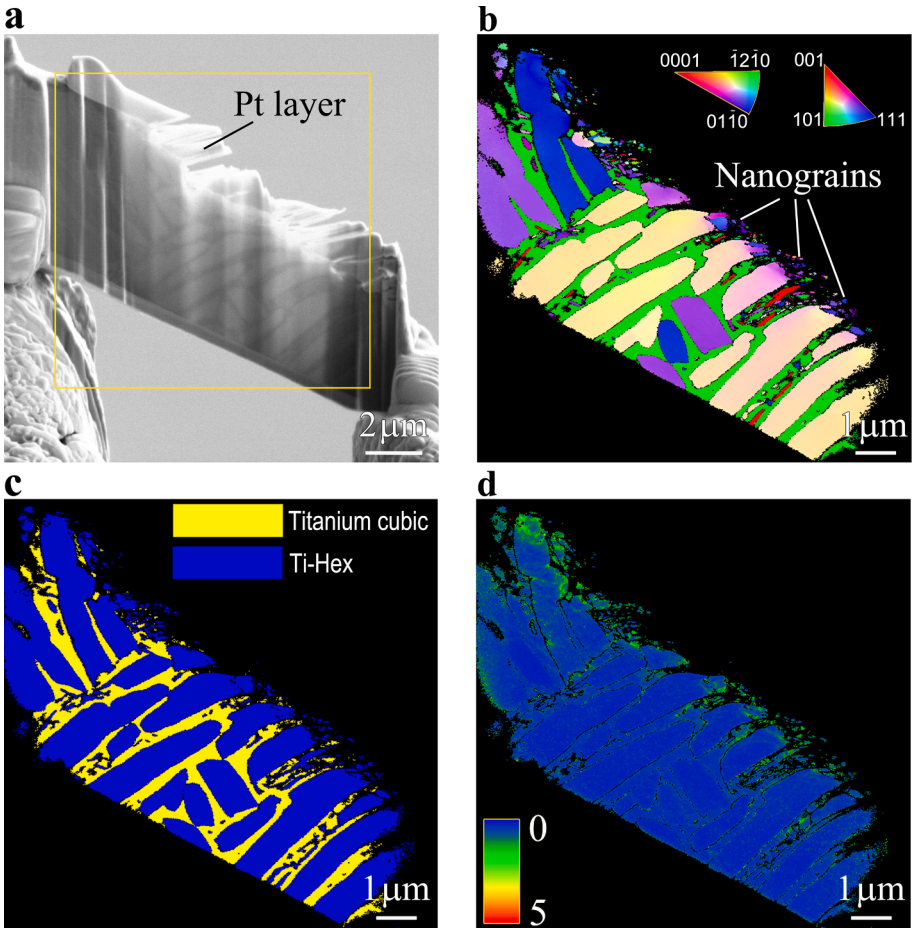


**Fig. 13.** SEM and TKD observation of extracted micro-sample 2 in the rough area in Fig. 7b. a: SEM observation of extracted sample; b-d: IPF, phase map, and KAM map of the rectangular region in a, respectively.

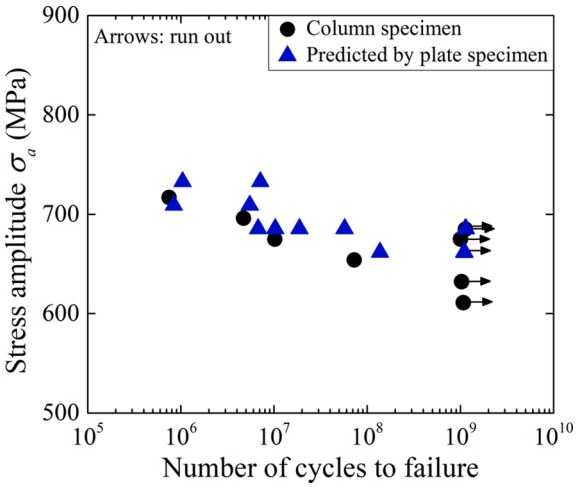


**Fig. 14.** Comparison of experimental fatigue strengths of smooth column specimens with predicted ones by Eq. (1) using the experimental data of smooth plate specimens.

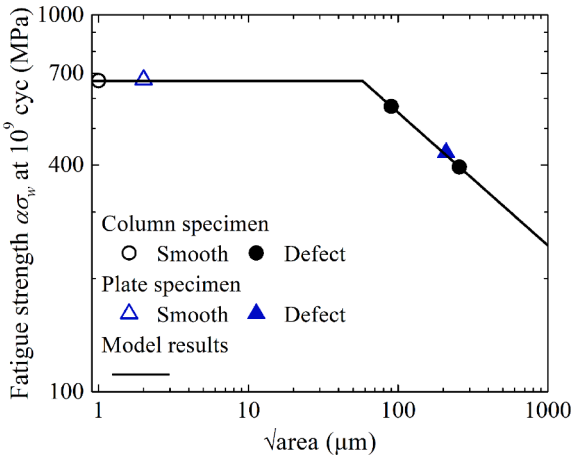


**Fig. 15.** Comparison of model results and experimental data for column specimens and plate specimens with and without artificial surface defects.

**Table 2**
Fatigue strength and defect size for column and plate specimens at $10^9$ cycles.

| Column specimen | | | Plate specimen | | |
|---|---|---|---|---|---|
| Specimen type | Fatigue strength (MPa) | Defect size (μm) | Specimen type | Fatigue strength (MPa) | Defect size (μm) |
| Smooth specimen | 669.5 | | Smooth specimen | 598.5 | |
| Specimen with defect A | 572 | 90 | Specimen with defect | 383.5 | 209 |
| Specimen with defect B | 395.5 | 256 | | | |

## CRediT authorship contribution statement

**Han Wu:** Visualization, Methodology, Investigation, Formal analysis, Writing - original draft, Writing - review & editing. **Weiqian Chi:** Formal analysis, Writing - original draft, Writing - review & editing. **Wei Xu:** Conceptualization, Writing - review & editing. **Wenjing Wang:** Conceptualization, Funding acquisition, Writing - review & editing. **Chengqi Sun:** Supervision, Methodology, Investigation, Funding acquisition, Formal analysis, Conceptualization, Visualization, Writing - original draft, Writing - review & editing.

## Declaration of Competing Interest

The authors declare that they have no known competing financial interests or personal relationships that could have appeared to influence the work reported in this paper.

## Data availability

Data will be made available on request.

## Acknowledgements

The authors acknowledge the help of Mr. Jian Sun and Dr. Gen Li in the Institute of Mechanics, Chinese Academy of Sciences in preparing the manuscript, and the support from the National Natural Science Foundation of China (91860112), the National Key Research and Development Program of China (2021YFB3703804) and the Science and Technology Research and Development Program of China State Railway Group Co., Ltd. (K2021J006).

## References

[1] Murakami Y. Metal fatigue: effects of small defects and nonmetallic inclusions. Oxford, UK: Academic Press; 2019.
[2] Sun C, Liu X, Hong Y. A two-parameter model to predict fatigue life of high-strength steels in a very high cycle fatigue regime. Acta Mech Sinica 2015;31(3):383–91.
[3] Zhang J, Li H, Yang B, Wu B, Zhu S. Fatigue properties and fatigue strength evaluation of railway axle steel: Effect of micro-shot peening and artificial defect. Int J Fatigue 2020;132:105379.
[4] Chi W, Wang W, Xu W, Li G, Chen X, Sun C. Effects of defects on fatigue behavior of TC17 titanium alloy for compressor blades: Crack initiation and modeling of fatigue strength. Eng Fract Mech 2022;259:108136.
[5] Li G, Sun C. High-temperature failure mechanism and defect sensitivity of TC17 titanium alloy in high cycle fatigue. J Mater Sci Technol 2022;122:128–40.

[6] Grad P, Reuscher B, Brodyanski A, Kopnarski M, Kerscher E. Mechanism of fatigue crack initiation and propagation in the very high cycle fatigue regime of high-strength steels. Scripta Mater 2012;67(10):838–41.
[7] Hong Y, Liu X, Lei Z, Sun C. The formation mechanism of characteristic region at crack initiation for very-high-cycle fatigue of high-strength steels. Int J Fatigue 2016;89:108–18.
[8] Su H, Liu X, Sun C, Hong Y. Nanograin layer formation at crack initiation region for very-high-cycle fatigue of a Ti–6Al–4V alloy. Fatigue Fract Eng Mater Struct 2017;40(6):979–93.
[9] Sun C, Song Q, Zhou L, Liu J, Wang Y, Wu X, et al. The formation of discontinuous gradient regimes during crack initiation in high strength steels under very high cycle fatigue. Int J Fatigue 2019;124:483–92.
[10] Chi W, Li G, Wang W, Sun C. Interior initiation and early growth of very high cycle fatigue crack in an additively manufactured Ti-alloy. Int J Fatigue 2022;160:106862.
[11] Jiang Q, Sun C, Liu X, Hong Y. Very-high-cycle fatigue behavior of a structural steel with and without induced surface defects. Int J Fatigue 2016;93:352–62.
[12] Wang Q, Bathias C, Kawagoishi N, Chen Q. Effect of inclusion on subsurface crack initiation and gigacycle fatigue strength. Int J Fatigue 2002;24:1269–74.
[13] Sun C, Lei Z, Xie J, Hong Y. Effects of inclusion size and stress ratio on fatigue strength for high-strength steels with fish-eye mode failure. Int J Fatigue 2013;48:19–27.
[14] Akiniwa Y, Miyamoto N, Tsuru H, Tanaka K. Notch effect on fatigue strength reduction of bearing steel in the very high cycle regime. Int J Fatigue 2006;28(11):1555–65.
[15] Chi W, Wang W, Li Y, Xu W, Sun C. Defect induced cracking and modeling of fatigue strength for an additively manufactured Ti-6Al-4V alloy in very high cycle fatigue regime. Theor Appl Fract Mec 2022;119:103380.
[16] Furuya Y. Specimen size effects on gigacycle fatigue properties of high-strength steel under ultrasonic fatigue testing. Scripta Mater 2008;58(11):1014–7.
[17] Shirani M, Härkegård G. Fatigue life distribution and size effect in ductile cast iron for wind turbine components. Eng Fail Anal 2011;18(1):12–24.
[18] Li Y, Song Q, Yang K, Chen Y, Sun C, Hong Y. Probabilistic control volume method for the size effect of specimen fatigue performance. Chin J Theor Appl Mech 2019;51(5):1363–71.
[19] Li C, Hu Z, Sun C, Song Q, Zhang W. Probabilistic control volume method for evaluating the effects of notch size and loading type on fatigue life. Acta Mech Solida Sin 2020;33(2):141–9.
[20] Zhang Z, Li Z, Wu H, Sun C. Size and shape effects on fatigue behavior of G20Mn5QT steel from axle box bodies in high-speed trains. Metals 2022;12:652.
[21] Murakami Y, Yokoyama NN, Nagata J. Mechanism of fatigue failure in ultralong life regime. Fatigue Fract Eng Mater Struct 2002;25:735–46.
[22] Nakajima M, Tokaji K, Itoga H, Shimizu T. Effect of loading condition on very high cycle fatigue behavior in a high strength steel. Int J Fatigue 2010;32(2):475–80.
[23] Sun C, Song Q. A method for evaluating the effects of specimen geometry and loading condition on fatigue life of metallic materials. Mater Res Express 2019;6(4):046536.
[24] Peng W, Xue H, Rui G, Peng Z, Hénaff G. The influential factors on very high cycle fatigue testing results. MATEC Web Conf 2018;165:20002.
[25] Song Q, Li Y, Wang L, Huang R, Sun C. Effect of rise and fall time on dwell fatigue behavior of a high strength titanium alloy. Metals 2019;9:914.
[26] Sun J, Peng W, Sun C. Mechanism of artificial surface defect induced cracking for very high cycle fatigue of Ti alloys. Eng Fract Mech 2022;272:108721.
[27] Sun C, Wu H, Chi W, Wang W, Zhang G. Nanograin formation and cracking mechanism in Ti alloys under very high cycle fatigue loading. Int J Fatigue doi: 10.1016/j.ijfatigue.2022.107331.
[28] Hu Y, Sun C, Xie J, Hong Y. Effects of loading frequency and loading type on high-cycle and very-high-cycle fatigue of a high-strength steel. Materials 2018;11:1456.
[29] Li Y, Song Q, Feng S, Sun C. Effects of loading frequency and specimen geometry on high cycle and very high cycle fatigue life of a high strength titanium alloy. Materials 2018;11:1628.
[30] Sun C, Chi W, Wang W, Duan Y. Characteristic and mechanism of crack initiation and early growth of an additively manufactured Ti-6Al-4V in very high cycle fatigue regime. Int J Mech Sci 2021;205:106591.
[31] Liu Y, Mahadevan S. Probabilistic fatigue life prediction using an equivalent initial flaw size distribution. Int J Fatigue 2009;31(3):476–87.
[32] Jesus J, Borges M, Antunes F, Ferreira J, Reis L, Capela C. A novel specimen produced by additive manufacturing for pure plane strain fatigue crack growth studies. Metals 2021;11(3):433.
[33] Bao H, McEvily A. On plane stress–plane strain interactions in fatigue crack growth. Int J Fatigue 1998;20(6):441–8.
[34] Tanaka K, Mura T. A Dislocation model for fatigue crack initiation. J Appl Mech 1981;48:97–103.
[35] Lavenstein S, Gu Y, Madisetti D, El-Awady JA. The heterogeneity of persistent slip band nucleation and evolution in metals at the micrometer scale. Science 2020;370(6513).
[36] Mughrabi H, Ackermann F, Herz K. Persistent slip bands in fatigued face-centered and body-centered cubic metals. In: Fong JT, editor. Fatigue mechanisms. ASTM STP 675. Philadelphia: American Society for Testing and Materials; 1979. p. 69–105.
[37] Weidner A, Amberger D, Pyczak F, Schönbauer B, Stanzl-Tschegg S, Mughrabi H. Fatigue damage in copper polycrystals subjected to ultrahigh-cycle fatigue below the PSB threshold. Int J Fatigue 2010;32(6):872–8.
[38] Wang C, Liu Y, Nikitin A, Wang Q, Zhou M. A general scenario of fish-eye crack initiation on the life of high-strength steels in the very high-cycle fatigue regime. Fatigue Fract Eng Mater Struct 2019;42(9):2183–94.
[39] Song Q, Sun C. Mechanism of crack initiation and early growth of high strength steels in very high cycle fatigue regime. Mater Sci Eng A 2020;771:138648.
[40] Zhang H-J, Yu F, Li S-X, He E-G. Fine granular area formation by damage-induced shear strain localization in very-high-cycle fatigue. Fatigue Fract Eng Mater Struct 2021;44(9):2489–502.
[41] Sajadifar SV, Wegener T, Yapici GG, Niendorf T. Effect of grain size on the very high cycle fatigue behavior and notch sensitivity of titanium. Theor Appl Fract Mec 2019;104:102362.
[42] Botvina LR, Petrova IM, Gadolina IV, Levin VP, Demina YA, Soldatenkov AP, et al. High-cycle fatigue failure of low-carbon steel after long-term aging. Inorg Mater 2010;46(14):1570–7.
[43] Miller K, O'Donnell W. The fatigue limit and its elimination. Fatigue Fract Eng Mater Struct 1999;22:545–57.
[44] Bathias C, Paris P. Gigacycle fatigue in mechanical practice. New York, USA: CRC Press; 2004.
[45] Xu W, Chen X, Gao Z, Li Y, He Y, Tao C. Fatigue behaviors of a titanium alloy in the VHCF regime based on a vibration-based bending fatigue test. Fatigue Fract Eng Mater Struct 2022;45(9):2549–62.
[46] Zhao X, Wu S, Bao J, Ao Ni, Peng W, Sun W. Experimental characterization and numerical modeling on the external impacting of high-speed railway axle EA4T steel. Eng Fail Anal 2021;125:105449.
[47] Gao J-W, Pan X-N, Han J, Zhu S-P, Liao D, Li Y-B, et al. Influence of artificial defects on fatigue strength of induction hardened S38C axles. Int J Fatigue 2020;139:105746.